Characterization of ENSO in a stratosphere-resolving version of the EC-EARTH model: comparison with observations and with the low-top version

Author: Mario Rodrigo Sanchez
Supervisors: Ileana Bladé Mendoza, ileanablade@ub.edu and Javier García Serrano, j.garcia-serrano@meteo.ub.edu
*Facultat de Física, Universitat de Barcelona, Diagonal 645, 08028 Barcelona, Spain.**

A stratosphere-resolving configuration (HIGH-TOP) of the EC-EARTH global climate model (GCM) is used to characterize the El Niño-Southern Oscillation (ENSO) and compare it to observations. Despite the state of the art stratosphere, HIGH-TOP still presents some biases in the seasonal cycle and in the ENSO spatial pattern common to other GCMs. The interannual peak in the Niño3.4 index power spectrum is broadly captured, but the model is biased towards lower frequencies. To assess the effects of a well-resolved stratosphere in the tropical Pacific and, in particular, on ENSO, HIGH-TOP is compared with a low-top version of the model (LOW-TOP). HIGH-TOP displays systematic and statistically significant higher interannual variability in the central-eastern Pacific, along with an improvement in the ENSO pattern of sea surface temperature (SST) anomalies. The comparison of the ENSO-induced tropospheric circulation anomalies reveals a strengthening of the eastern Pacific intertropical convergence zone (ITCZ) in HIGH-TOP with respect to LOW-TOP. Additionally, in the equatorial eastern Pacific, HIGH-TOP correctly simulates anomalous upward motion, while LOW-TOP simulates anomalous downward motion that enhances the climatological Walker circulation. The stronger ITCZ and the anomalous ascent in the eastern equatorial Pacific in HIGH-TOP are consistent with the higher total interannual variability in SST and precipitation in HIGH-TOP. Hence, incorporating a well-resolved stratosphere in the EC-EARTH model yields a more realistic representation of the variability in the central-eastern Pacific and tropical ENSO pattern.

I. INTRODUCTION

Earth's climate is a coupled dynamical system ruled by a set of equations that has no analytical solution, so numerical simulations are the only practical manner to accurately simulate the present climate in order to improve our understanding. Another application of these simulations is to predict possible climate modifications. Because there are strong interactions between the atmosphere and the ocean, atmospheric general circulation models (AGCMs), which treat SST as an external forcing, are not appropriate for studying coupled climate dynamics. Instead, coupled climate models, also known as Global Climate Models or General Circulation Models (GCMs), are used; they also include the other components of the climate system, such as the ocean, land surface, biosphere and cryosphere (*Hazeleger et al.* (2011)).

Among all the coupled climate phenomena, ENSO is the major interannual climate variability source. Its ocean component consists of an irregular oscillation of the SST with a characteristic period between 2-7 years that occurs in the central-eastern equatorial Pacific. These anomalies generally begin along the west coast of Peru in late spring-early boreal summer, but over the course of the following months spread westward along the equator to produce large-scale SST anomalies over much of the equatorial Pacific that peak in boreal winter (DJF). For most events, these anomalies display different signs between the central-eastern tropical Pacific - the cold tongue - and the tropical western and extra tropical Pacific, so that the pattern exhibits a horseshoe-like shape. El Niño (La Niña) is how the warm (cold) phase of this oscillation is referred to. Its atmospheric component, the Southern Oscillation, is characterized by an interannual oscillation in tropical sea level pressure between the Western and Eastern Pacific, which modifies the intensity of the easterly trade winds over the tropical Pacific (*Wang and Picaut* (2004)). It was Bjerknes who recognized that there is a close connection between both components and that they are two different aspects of the same phenomenon. He postulated a positive ocean-atmosphere feedback (which later adopted his name) involving the zonal atmospheric circulation in the equatorial Pacific or Walker circulation, surface SSTs and equatorial upwelling that enhances the development of both ENSO phases. An initial positive (negative) SST anomaly in the equatorial eastern Pacific reduces (increases) the zonal SST gradient which then weakens (strengthens) the trade winds in the Walker circulation, which in turn further warms the SST in the eastern Pacific, via reduced evaporative cooling and reduced supply of upwelled cold water. This positive feedback eventually leads the equatorial Pacific to a full-blown warm (cold) phase of ENSO.

In response to changes in the Walker circulation there are also changes in the tropical deep convection and the Hadley circulation. Tropical deep convection occurs over SSTs above 27°C, so in neutral conditions it is located over the warm pool in the western Pacific. During a

* Electronic address: mrodrigo@meteo.ub.edu

warm (cold) phase of ENSO, when the Walker circulation weakens (strengthens) and the central-eastern Pacific becomes anomalously warm (cold), the deep convection shifts eastward (westward) towards the central Pacific (Maritime Continent and the Indian Ocean), as shown in Fig.1b (Fig.1a). The zonal circulation in the Tropics, i.e., the Walker cell in the Pacific, and the Hadley circulation are connected through the regions of vertical motion in the Tropics. This link represents the tropical branch of the atmospheric connection between tropical and extra-tropical SSTs, which is known as the atmospheric bridge, as described by *Klein et al.* (1999) and deeply investigated by *Wang* (2001) in the Pacific region. Changes in the Walker circulation can thus induce changes in the Pacific Hadley circulation and vice versa. For example, for a warm phase of ENSO, when the Walker circulation is weakened and deep convection is shifted towards the central Pacific, the Hadley circulation is reinforced in that region, while it is replaced by a thermally indirect cell in the far western Pacific, consistent with the anomalous downward motion over the tropical western Pacific.

So far, all the ENSO-induced dynamics discussed here concern the ocean and the troposphere, but it is also known that ENSO affects the strength and variability of the stratospheric circulation in both the tropics (i.e. tropical upwelling) and the extra-tropics (i.e. polar vortex) (*Domeisen et al.* (2019) for a review). These impacts involve changes in the mean circulation and in the upward wave propagation. The positive phase of ENSO is associated with a warming and weakening of the polar vortex, while a cooling can be observed in the tropical lower stratosphere. This cooling is partly explained by the rising of the tropical air from the region of enhanced convection, which then crosses the tropopause and penetrates into the warmer stratosphere. There is another contribution associated with the strengthened Brewer-Dobson circulation, which refers to the stratospheric Lagrangian equator-to-pole overturning circulation driven by tropospheric vertical wave propagation and breaking. El Niño leads to more wave breaking, which enhances the tropical upwelling and the polar downwelling. The latter contributes to the warming in the polar vortex, while the former explains some of the cooling in the tropical lower stratosphere. For La Niña these anomalies are often opposite. Changes in the polar stratosphere in turn may affect mid-latitude surface weather and climate over large areas of the globe and the tropospheric ENSO teleconnection itself.

Understanding ENSO impacts in the stratosphere can therefore be useful for sub-seasonal to seasonal prediction. In this line of research, *Cagnazo and Manzini* (2009) and *Ineson and Scaife* (2009) have focused on the influence of the stratosphere on ENSO teleconnections to the extra-tropics, in particular, to the North Atlantic and European region. There has been less focus on the ENSO influence on the tropical stratosphere with a few exceptions, such as *Randel et al.* (2009), who found that ENSO events are linked to variations in zonal mean temperature and ozone composition in the tropical lower stratosphere in both models and observations. These variations are again tied to fluctuations in the tropical upwelling generated by ENSO. *Taguchi* (2010) studied the impact of ENSO on the largest source of tropical stratospheric variability, the quasi-biennial oscillation (QBO) of equatorial stratospheric zonal winds, and found that the wind anomalies associated with the QBO propagate downward faster during El Niño than during La Niña, due to the modulation of the waves generated within the troposphere that then propagate up and force the QBO. Despite extensive research on the interaction between ENSO and the stratosphere, many issues remain to be understood, in particular about the impact of the stratosphere on ENSO.

The purpose of this research is to study the influence of having a well-resolved stratosphere on the tropical Pacific mean atmospheric circulation and ENSO by comparing two GCM simulations under two configurations: a high-top, well-resolved stratosphere (HIGH-TOP or HT) and a low-top, poorly-resolved stratosphere (LOW-TOP or LT). First, we assess the performance of the HT simulation by comparing the basic state, climatology and variability, in the Tropical Pacific and the spatio-temporal characteristics of ENSO with observations. Second, both configurations are compared in order to assess the impact of a high-resolution stratosphere. Then, we focus on ENSO-induced tropospheric dynamics to further understand the differences between configurations.

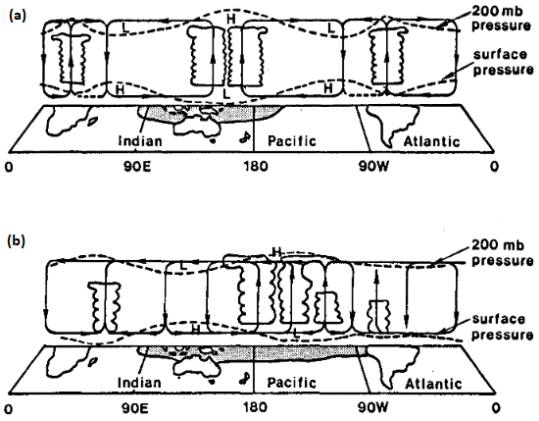

Figure 1. *Schematic diagrams of the zonal cells along the equator, the Walker cell in the Pacific, for (a) La Niña and (b) El Niño conditions. The shaded areas indicate SST warmer than* 27° *C. From Webster and Chang (1988)*

II. DATA AND METHODOLOGY

A. Data, model and experimental set-up

The data sets used for the SST and the precipitation are: Hadley Centre Sea Ice and Sea Surface Temperature data set version 1 (HadISST) and Extended Reconstructed Sea Surface Temperature (ERSST); CPC Merged Analysis of Precipitation (CMAP) and Global Precipitation Climatology Center (GPCP). The period considered is from 1979 to 2019 for both variables, otherwise specified.

The GCM used is the European Consortium EC-EARTH climate model version 3.1, which is based on the operational seasonal forecast system of the European Center for Medium-Range Weather Forecasts (ECMWF). Its atmospheric component is the Integrated Forecasting System (IFS) cycle 36r4, which is a primitive equation model with fully interactive cloud and radiation physics. The model can be run at different resolutions. Here we use a horizontal spectral truncation of T255 (triangular truncation at wavenumber 255) and the vertical resolution is different for the two experiments. The radiative forcing for both experiments is fixed at a forcing representative of present climate (i.e. 2000). For the ocean model EC-EARTH uses the NEMO3.6, which consists of an ocean general circulation model (ORCA1) plus a sea ice model (LIM3). It has a horizontal resolution of about 1° and 42 layers. It is important to point out that the horizontal resolution increases up to one third of a degree near the equator to resolve equatorial planetary waves, which are important for ENSO (*Madec* (2008)). The last important component of the model is the interactive atmosphere-sea-ice coupler which is applied across the entire globe, including the polar regions. The IFS and NEMO3.6 are coupled with the Ocean Atmosphere Sea Ice Soil version 3 (OASIS3; *Valcke* (2006)) coupler. These couplings take place every 3 h, while the time step for all the other components is 45 min (*Hazeleger et al.* (2011)).

Two 100-year long experiments after 30 years of spin-up are compared. A HT simulation with the top at 0.01hPa and 91 vertical levels and a parallel LT version with the top at 5hPa and 62 vertical levels. The HT experiment is the control experiment and the LT experiment is used to assess the impact of resolving the stratosphere. Since the CO_2 concentration is constant in the simulations, the focus of this study is internal climate variability. Therefore, all observational data sets are detrended before the analysis of the basic state and ENSO characterization.

B. Methodology

To analyze the basic state, the DJF climatology and standard deviation of SST and precipitation are presented for the observations together with the differences between HT and observations and HT minus LT. Two observational data sets are used for each variable to account for the observational uncertainty. The statistical tests to assess the significance of the differences in the means and standard deviation are a Student test with the null hypothesis of equal means and a Fisher test with the null hypothesis of equal standard deviations.

For the spatio-temporal characterization of ENSO we use the Niño3.4 index, which is the anomalous averaged temperature in the region 3.4 of the tropical Pacific ocean, as illustrated in Fig. 2. In particular: for the analysis of the seasonal cycle, the Niño3.4 monthly standard deviation is computed for both experiments and observations and the significance of the differences is tested with a Fisher test. To obtain a spatial pattern, regression maps of the SST anomalies onto the standardized Niño3.4 index for DJF are computed and the correlations are tested using a Student test with the null hypothesis of correlation coefficient equal to zero. For the power spectral density (or simply power spectrum), a Fourier Transform is applied to the Niño 3.4 monthly time series. In this case, the period considered in the SST data sets is from 1919 to 2019 in order to have the same sampling as in the experiments. The power spectrum has been computed after partitioning the time series in three segments of 50 years with an overlap of 25 years and then averaging the Fourier estimates, which yields 6 degrees of freedom for the spectral estimate. This computation is sensitive to the length of the segment, so the criteria used was to have segments with the largest possible sampling, that is, 50 years. The variance of each time series is used to compute the best fit red noise spectrum, with decorrelation time $\tau = 6.1$ months assumed for red noise. Then a Fisher test is used to find the variance for each spectral estimate at the 95% confidence upper-bound.

In order to study ENSO dynamics, regression maps of several tropospheric circulation fields onto the standardized Niño3.4 index are computed using the same statistical test as for the spatial pattern. These fields are the velocity potential and the divergent wind at 200 hPa and 850 hPa and the omega velocity at 500 hPa (with the sign changed so that positive values correspond to upward motion). For the differences in regression coefficients the statistical test uses the null hypothesis of equal correlation coefficients. In all statistical tests the probability that the null hypothesis can be rejected is assessed at the 95% confidence level.

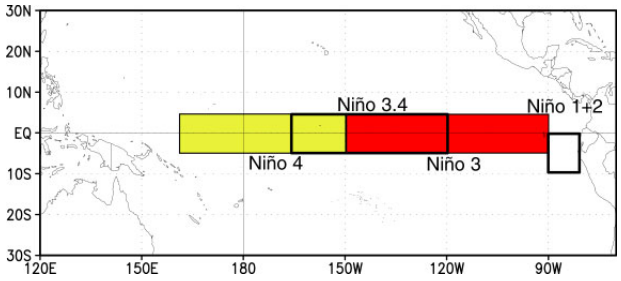

Figure 2. *El Niño regions from NOAA Climate Prediction Center.*

III. RESULTS

A. Tropical Pacific and ENSO characterization

1. HT versus observations

As the basic state determines ENSO, we first compare the long-term mean (climatology) and standard deviation (variability) in HT and observations for DJF. SST and precipitation are chosen for this characterization, since they are key variables for both the oceanic and atmospheric components of ENSO.

Figures 3a and 3d show the basic state in HadISST. In the target region -the tropical Pacific- the SST climatological gradient is mainly zonal with the cold tongue in the eastern Pacific and the warm pool in the western Pacific (*Deser et al.* (2010)). There is also a sharp contrast in variability between both regions, with the largest values of SST standard deviation in the cold tongue region and relatively small variability in the warm pool. Figure 3b shows that overall HT is warmer than HadISST, except in the subtropics and in the central North Atlantic, and particularly so in the tropical band, including the tropical Pacific. The largest differences are found in the Humboldt or Peru current and in the California current, the eastern boundary currents of the Pacific Ocean. These regions overlap with those in which HT simulate weaker easterlies than observed (not shown). This suggest that where the trade winds (easterlies) are weaker in the model the turbulent heat flux, mainly latent, is reduced, and so is the heat released from the ocean to the atmosphere (*Deser et al.* (2010)). Thus, those regions are associated with a warmer ocean, as found in 3b. This mechanism is just one contribution to the differences in SST climatology between observations and HT, because in the regions where the trade winds are stronger in HT the differences in SST climatology are still positive, but smaller. The comparison of standard deviation in Figure 3e shows that the cold tongue is meridionally narrower in the central Pacific in HT, particularly in the Northern Hemisphere, and more extended towards the western Pacific. The differences in meridional extent are even larger with respect to ERSST, while the differences in the westward extent are reduced (see Fig. 8b in the appendix).

Figure 3g shows the precipitation climatology of CMAP. In the western Pacific, over the Maritime Continent, precipitation is high, associated with convection over the Pacific warm pool. From there, the ITCZ extends eastward north of the equator, while in the Southern Hemisphere the south Pacific convergence zone (SPCZ) extends southeastward. In the cold tongue region there is little precipitation, since this region is characterized by descending motion in the Walker cell (see Figs. 1 and 7). The relationship between precipitation and SST is evident, with large amounts of precipitation located over regions of SST warmer than 27°C (see Fig.3a). The standard deviation of CMAP precipitation is maximum in the central-western Pacific (3j), associated with shifts of the warm pool deep convection and both SPCZ and ITCZ convergence zones. This pattern is very similar to that of the standard deviation of surface zonal winds in the tropical Pacific (not shown), because changes in deep convection and lower-tropospheric wind convergence are linked by mass continuity. Turning now to the model, HT shows larger rainfall than observed in the Pacific side of the warm pool and in the ITCZ along the central-western Pacific (Fig. 3h). These differences are even larger with respect to GPCP (Fig. 8c in the appendix). The precipitation in the SPCZ is shifted towards the Maritime Continent compared to both observational data sets, which is consistent with the shift in the convergence of the surface winds (not shown) and is a typical bias of GCMs (*Kurcharski et al.* (2015)). Figure 3k shows that there is more simulated variability than observed in the ITCZ in the western-central Pacific, but reduced variability in all the central Pacific south of the equator and along the eastern Pacific ITCZ.

In order to study the SST variability related to ENSO, the seasonal cycle of the Niño3.4 standard deviation is examined first (Fig. 4). Notice that only data since 1960 are used, because of the improvement in the SST coverage and quality (*Deser et al.* (2010)). There are no statistically significant differences in the standard deviation of the Niño3.4 index between observational data sets (black stars in Fig.4); hence in the following we jointly refer to them as observations. When comparing the spatial pattern of ENSO between the simulations and observations, HadISST is used because of the higher spatial resolution (1° latitude by 1° longitude), compared to ERSST (2° latitude by 2° longitude). Note that there are no also statistically significant differences in the basic state between both observational data sets (Figs.8a and 8.b in the appendix).

The observed seasonal cycle (black and grey) of Niño3.4 shows maximum variability in December and

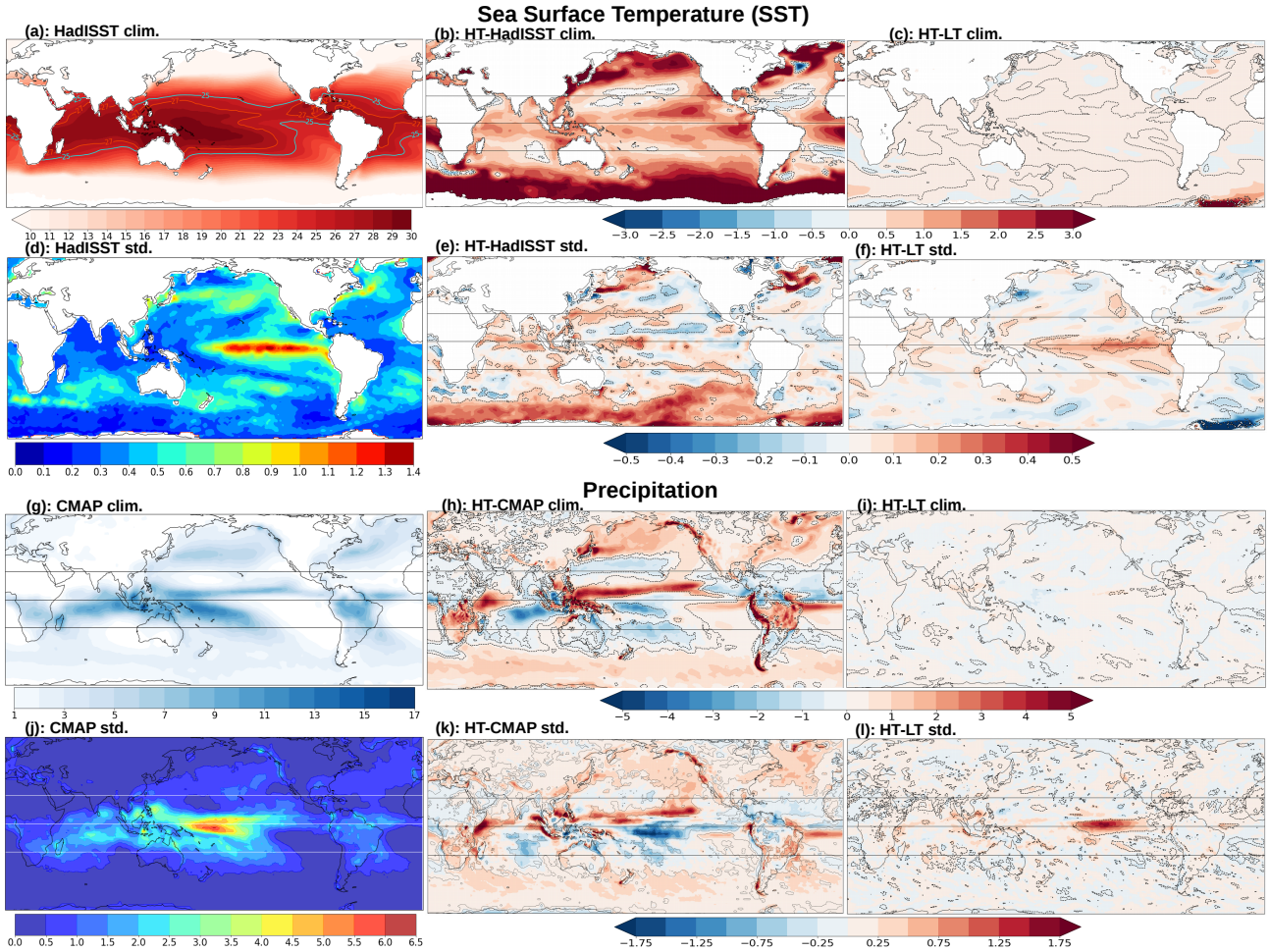

Figure 3. *(a) HadISST climatology (°C); (b) HT minus HadISST; (c) HT minus LT; (d), (e) and (f) as in (a), (b) and (c) but for standard deviation, respectively; (g) CMAP climatology (mm/day); (h) HT minus CMAP; (i) HT minus LT; (j), (k) and (l) as (g), (h) and (i) bur for standard deviation. Dashed contours denote significant differences in climatology and standard deviation using a Student and a Fisher test, respectively. Solid horizontal lines in some maps are the equator and both tropics.*

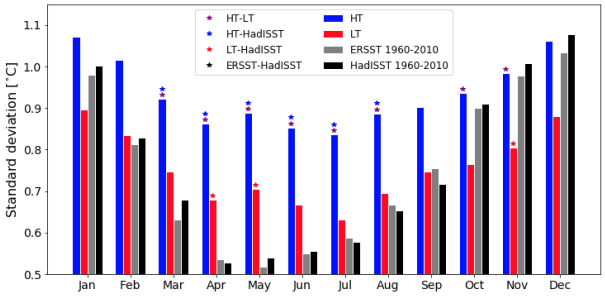

Figure 4. *Niño3.4 SST index variability for HadISST, ERSST, HT and LT. Stars denote significant differences using a Fisher test.*

minimum in April and May (Fig. 4). HT (blue) simulates a biased seasonal cycle with a maximum in January and a minimum in July, which is a systematic error in EC-EARTH (*Yang et al.* (2010)). HT also substantially overestimates the variability during spring and early summer, which appears to be a common bias in climate models (*Guilyardi et al.* (2009)). On the other hand, HT captures the observed variability from October to December.

As stated in the introduction, the study is focused on DJF because it is the season of the peak and mature phase in the ENSO cycle (Fig.4). To spatially characterize ENSO at this phase, its pattern is diagnosed with a regression map of SST anomalies onto the Niño3.4 index (Fig. 5). HadISST shows the canonical signature of ENSO (*Chang and Battisti* (1998)), for the El Niño phase: a pattern dominated by positive anomalies over the central-eastern tropical Pacific, i.e. along the cold tongue region, that extends along the coast into mid-latitudes in both hemispheres, surrounded by horseshoe-shaped negative anomalies that stretch from the warm pool into the extra-tropics. HT is capable of simulating the ENSO pattern reasonably well (Fig.5b and 5c), although the tongue of warm SST anomalies is

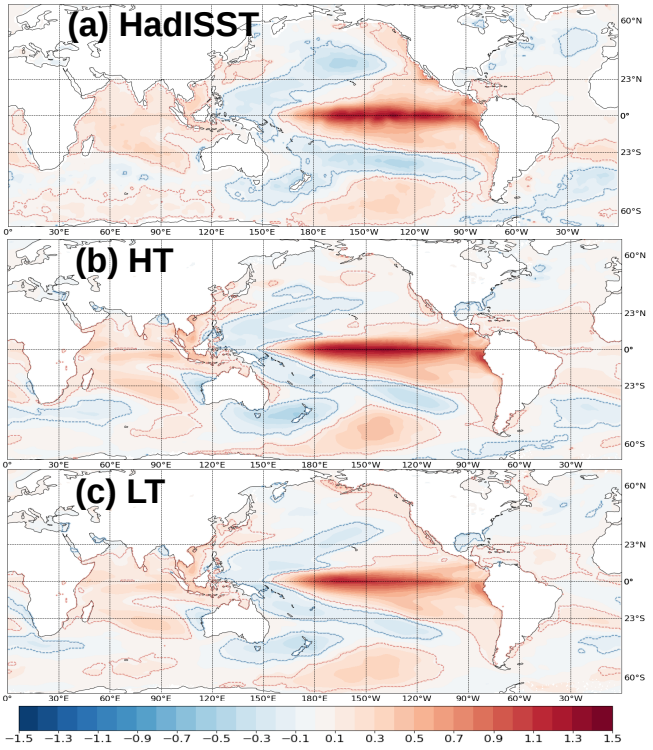

Figure 5. *Linear regression of the DJF SST anomalies (shading) onto the Niño3.4 index for: (a) HadISST; (b) HT; (c) LT. Units are Celsius degrees. Regions where the correlation coefficients are significantly different from zero are limited by contours.*

meridionally narrower and slightly shifted towards the western tropical Pacific compared to observations, both biases being again common to climate models (*Guilyardi et al.* (2009)). HT also fail to capture the amplitude of the ENSO teleconnection to the North Pacific, which is associated with changes in the Aleutian low (*Alexander et al.* (2002)).

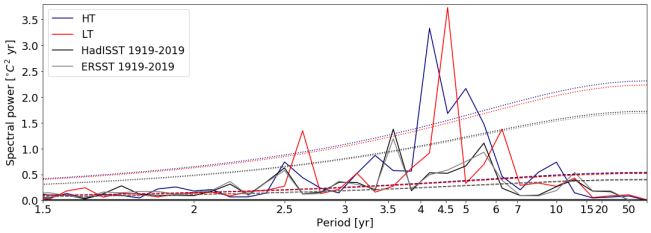

Figure 6. *Power spectral density of the Niño3.4 time series. The best fit red noise spectrum (dashed) and its* 95% *confidence bound (dotted) for HadISST (black), ERSST (grey), HT (blue) and LT (red).*

As can be seen in Figures 9a and 9b (appendix), the time series of the Niño3.4 index in observations and HT are very similar in terms of the dominant frequency of ENSO events. For a more detailed analysis and to more accurately temporally characterize ENSO, the power spectrum of the Niño3.4 indices has been computed (Fig.6). The power spectrum in observations (black and grey) displays a statistically significant peak at 3.5 years within the well-known interannual 2-6 years band of enhanced power (*Guilyardi et al.* (2009)). HT (blue) reproduces the irregular character of the tropical oscillation, with separate significant peaks between 4 and 5 years. This bias towards lower frequencies is common to climate models (*Kurcharski et al.* (2015) and *Guilyardi et al.* (2009)).

2. HT versus LT: sensitivity to a well-resolved stratosphere

For both variables considered in Figure 3, the differences in climatology between the HT and LT experiments are one order of magnitude smaller than the differences with observations. The differences are also smaller than the typical values of standard deviation, thus indistinguishable from internal variability and not significant (Figs. 3c and 3i). However, HT displays systematic and statistically significant increased SST and rainfall variability in the central-eastern Pacific (Figs. 3f and 3l). Thus, the negative HT biases in precipitation variability in the central Pacific south of the equator and along the ITCZ in the eastern Pacific (Fig. 3k) are even larger in LT (see Fig. 3l). Notice that the SST and the precipitation are dynamically related, as more SST variability is linked to more variability in precipitation by thermal forcing and enhancement of convection. The basic idea is that warm (cold) SSTs induce low (high) pressures over the SST anomalies, and the pressure perturbations subsequently force low-level convergence (divergence) of moisture, which produces convective precipitation. Consistent with the differences in SST standard deviation (Fig.3f), HT shows higher ENSO anomalies than LT in the cold tongue region (Fig. 5), yielding an improved representation of the pattern.

A comparison of the seasonal cycle of the Niño3.4 standard deviation (Fig.4) shows that HT (blue) better captures the observed variability from October to December although LT (red) represents it more accurately in late summer (July to September). Furthermore, HT systematically exhibits more variability than LT, between 15-20% depending on the season. For winter (DJF) these results are consistent with the significant differences in standard deviation over the tropical Pacific (see Fig. 3f). Nonetheless, notice that boreal winter is the only season for which the simulated and observed differences in the Niño3.4 standard deviation are not significant (purple stars), as the largest differences in SST variability are confined to the eastern Pacific, outside the Niño3.4 region (cf. Figs. 3f and 2).

The power spectrum in the LT experiment also

displays the bias towards lower frequencies in the interannual range with a prominent significant peak at 4.5 years. Additionally, there is another significant peak with a period slightly longer than 2.5 years, which is not observed.

Overall, HT systematically displays higher variability than LT in the central-eastern Pacific, consistent with the improved representation of the ENSO pattern. To further investigate the differences between configurations, in the next section we study the ENSO-induced tropical circulation.

B. ENSO dynamics

To better understand the tropical circulation associated with ENSO, we analyze the divergent circulation, in particular: the velocity potential at lower levels (850 hPa) and upper levels (250 hPa) and the vertical velocity at 500 hPa (omega). We first consider the DJF climatology of the divergent circulation. As the objective of this section is not to evaluate the differences in the basic state, but the anomalous circulation during ENSO in the model, only HT is shown in this section. The differences in climatology between both experiments are shown in Figures 10a-c (appendix).

As the divergent wind ($\vec{v_\chi}$) derives from the gradient of the velocity potential ($\vec{v_\chi} = \nabla\chi$), centers of negative velocity potential (blue shading) are associated with divergent outflow, while positive values (red shading) are related to convergent inflow. Figures 7a-c show that lower-tropospheric convergence collocates with upper-tropospheric divergence, associated with upward motion, here illustrated with negative omega velocity values in middle troposphere (recall sign change). These large-scale baroclinic structures are readily understood from the continuity equation (*Wang* (2001)). The western (eastern) tropical Pacific is dominated by deep convection and ascending motion (inhibition of convection and descending motion) linked to the Pacific warm pool (cold tongue); cf. Figures 7a-c, 3a. Associated with these patterns is the east–west circulation cell along the equator, the zonal Walker circulation. The air ascends in the western Pacific (Fig. 7b), flows eastward in the upper troposphere (Fig. 7a), sinks in the eastern Pacific (Fig. 7b), and returns to the western Pacific in the lower troposphere (Fig. 7c). Together with the widespread ascent in the western tropical Pacific, there is a narrow band of upward vertical motion over the central-eastern Pacific around 10°N, which corresponds to the local ITCZ. As depicted in Figures 7a–c, the meridional circulation in the western Pacific is different from that in the eastern Pacific. In the west, there is, as one would expect from general principles, a single thermally direct Hadley cell with air rising south of the equator (7.5°S), poleward flow in the upper troposphere, convergence at latitudes between 30°-40°N and return flow to the Tropics in the lower troposphere. In the east, the tropical meridional circulation is weaker and less straightforward. By examining a vertical section of the meridional flow in this region (not shown) it can be inferred that there are two Hadley cells with a common upward branch in the NH, in the ITCZ region (7.5°N), with descent over the subtropical high and in the equatorial eastern Pacific (consistent with *Wang* (2001)).

Figures 7d-f show the linear regression of the Niño3.4 index with the circulation fields considered above, again only for HT. Figures 10g-i (appendix) show the same analysis but for LT, in order to ease the description of the differences between both experiments discussed below. Associated with El Niño conditions (Fig. 5), the deep convection and the related Walker circulation are shifted towards the central-eastern Pacific following the relaxation of the trade winds and the anomalous warming of the cold tongue (see Introduction). This is illustrated here by the zonal displacement of the region of lower-tropospheric convergence and upper-tropospheric divergence (Fig.7d-f) and ascending motion (Fig.7e) and the upper-tropospheric divergence (Fig.7d). Tightly linked to the ENSO-induced shift in the deep convection, the Hadley circulation also moves eastward, showing upper-tropospheric convergence and descending motion in the subtropics at around 160°E, i.e., a longitudinal shift of about 30°. On the other hand, the local ITCZ at around 140°W moves equatorward generating an anomalous dipole of vertical velocity (Fig.7e) and precipitation (not shown).

Differences in the ENSO-related tropical circulation between the experiments are shown in Figures 7g-i. First, in the off-equatorial eastern Pacific there is a dipole in the vertical velocity HT-LT difference that projects on the anomalous dipole shown in Figure 7e, which reflects a more pronounced ITCZ shift in HT. In addition, in contrast to HT (Fig.7e), LT simulates anomalous descending motion along the eastern equatorial band (see Fig.10h in the appendix) in line with the stronger downward branch of the climatological Walker circulation (cf. Fig.7b and Fig.10b). Together, the stronger ITCZ change and the positive anomalous ascending motion in the eastern equatorial band in HT are consistent with higher interannual variability in that simulation, as can be seen in Figure 10e. Note the agreement between the regions of significant differences in variability of vertical velocity (Fig. 10e) and precipitation (Fig. 3l). Second, in the central-western North Pacific at around 30°N, there is a zonal dipole in the differences of vertical velocity (Fig. 7h), which indicates a stronger and slightly westward shifted descending branch of the Hadley cell in HT. This is consistent with the upper- and lower-tropospheric circulation differences, as depicted in Figures 7g and 7i, respectively, which also reflects a higher interannual variabil-

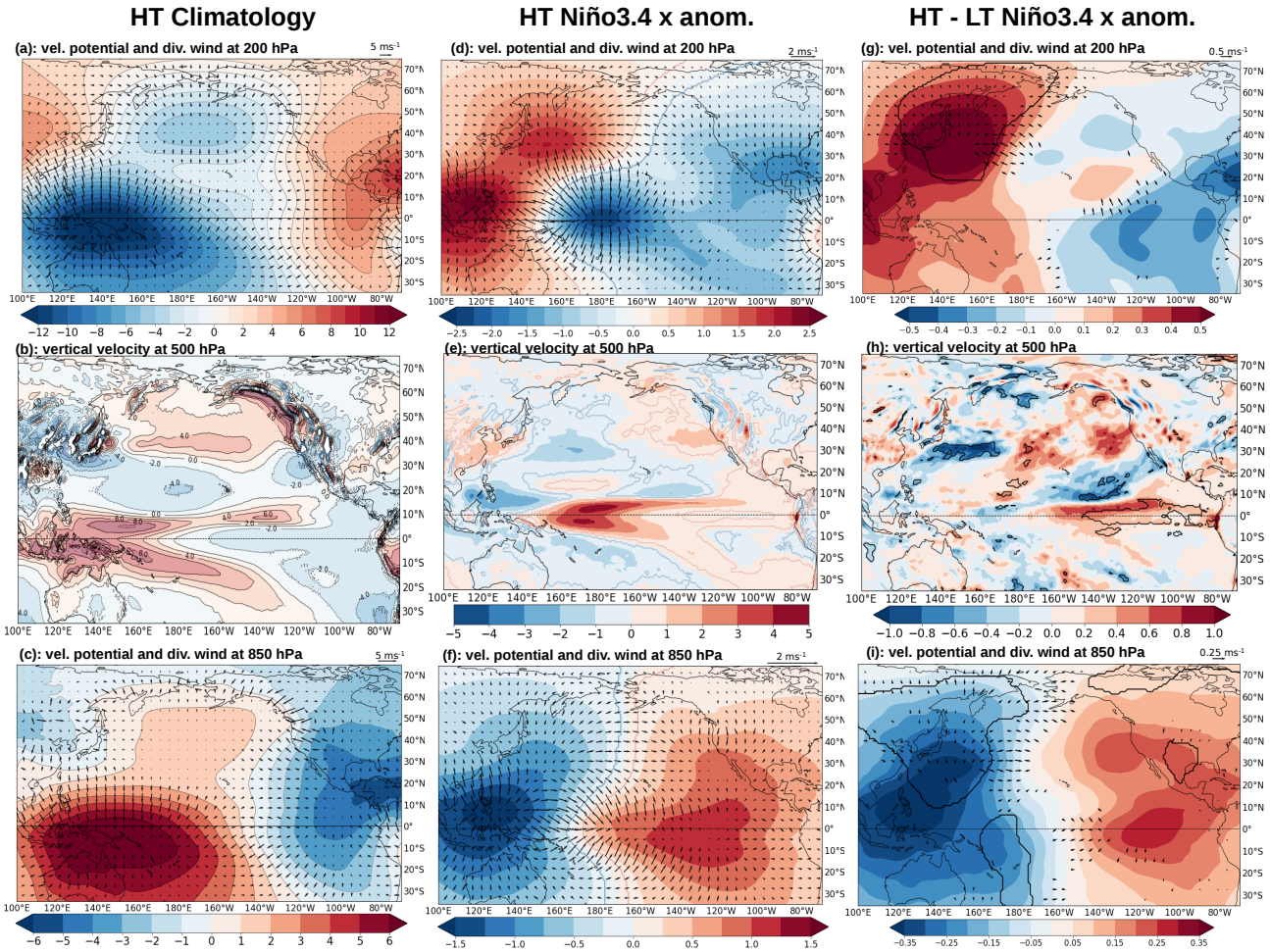

Figure 7. *(a), (b) and (c) DJF climatology in the HT experiment of 200 hPa velocity potential ($10^6\ m^2 s^{-1}$) and divergent wind (ms^{-1}), 500 hPa vertical velocity ($10^{-2}\ Pas^{-1}$) and 850 hPa velocity potential ($10^6\ m^2 s^{-1}$) and divergent wind (ms^{-1}), respectively. (d), (e) and (f) DJF linear regressions of the same variables as in (a), (b) and (c) onto the Niño3.4 index. Regions inside contours and the wind vectors plotted have significant correlations different from zero. (g), (h) and (i) HT minus LT of (d), (e) and (f), respectively. Regions inside contours and the wind vectors plotted have statistically significant different correlation coefficients in HT and LT. The vertical velocity is the negative of the pressure vertical velocity, i.e., positive values indicate upward motion.*

ity in the meridional divergent circulation (Figs.10d and 10f).

IV. CONCLUSIONS

The findings of this study may be summarized as follows:

1. HT simulates significantly warmer climatological SSTs than observations in the tropical Pacific. It also displays larger rainfall than observed in the Pacific side of the warm pool and over the ITCZ along the central-western Pacific.

2. The variability in SST and precipitation in the tropical Pacific is shifted towards the Maritime Continent in HT with respect to observations. The same occurs in the climatological SPCZ.

3. HT presents biases in the ENSO seasonal cycle and spatial pattern common to other state of the art GCMs: a temporal shift in the timing of maximum and minimum variability, an excess of variability in late spring and early summer and a cold tongue that is too narrow meridionally and slightly shifted towards the central-western Pacific.

4. The power spectrum in EC-EARTH reproduces the irregular character of the tropical oscillation but it is biased towards lower frequencies, which is common to other GCMs.

5. The differences in climatology of SST and precipitation between the HT and LT experiment are indis-

tinguishable from internal variability and not significant. However, HT displays systematic and statistically significant higher interannual variability in the central-eastern Pacific. The increased interannual variability in SST is consistent with an improvement in the amplitude of the ENSO pattern. HT also shows increased variability in precipitation associated with zonal displacements of the warm pool deep convection together with latitudinal shifts of the ITCZ.

6. The ENSO-induced circulation analysis reveals a stronger ITCZ change and positive anomalous ascending motion in the eastern equatorial Pacific in HT, which are consistent with the higher total interannual variability in HT.

Even though the ENSO-induced circulation has not been explicitly compared with observations, we can make the argument that the HT simulation produces an improvement in the ENSO anomalous circulation in EC-EARTH. First, the stronger HT anomalies are consistent with the higher and more realistic interannual variability in SST and precipitation in HT (cf. Figs. 3e with 3f and 3k with 3l). Second, *Wang* (2001) and *García-Serrano et al.* (2017) studied the observed atmospheric circulation cells associated with ENSO and found that for the mature phase of ENSO there is anomalous upward motion in all the central-eastern equatorial Pacific in line with the HT circulation.

The effect of having a well-resolved stratosphere in the EC-EARTH model is evident in the enhanced variability in the central-eastern tropical Pacific for all variables considered here. But further research is needed to understand the link between the resolution in the stratosphere and the enhanced tropospheric variability in this particular region. In the review of *Domeisen et al.* (2019), it is suggested that the QBO in tropical stratospheric zonal winds may have a possible downward influence on the tropical tropospheric precipitation. We know that only the HT configuration simulates a QBO (Fig.11 appendix; see *Palmeiro et al.* (2020)). A possible hypothesis for future research could be that the presence of a QBO modulates the deep convection in the tropical Pacific and impacts its variability (Fig.3l). Along this line of research, there is another available HIGH-TOP experiment but with the atmospheric circulation nudged to climatology above 10 hPa (NUDG) with which we plan to isolate the impact of including stratospheric variability (HT vs NUDG).

ACKNOWLEDGMENTS

Discussion with Javier García Serrano and Ileana Bladé Mendoza provided constructive comments and suggestions to improve the manuscript. This research was supported in first place by my parents and by the MASTER+UB scholarship thanks to the involvement of Ileana Bladé Mendoza and Javier García Serrano.

REFERENCES

Alexander, M. A., I. Bladé, M. Newman, J. R. Lazante, N.-C. Lau, and J. D. Scott, The atmospheric bridge: The influence of ENSO teleconnections on air-sea interaction over the global oceans, *J. Clym.*, *15*, 2205–2231, 2002.

Cagnazo, C., and E. Manzini, Impact of the stratosphere on the winter tropospheric teleconnections between ENSO and the North Atlantic and European region, *Ame. Meteor. Soc.*, *22*, 1223–1238, 2009.

Chang, P., and D. Battisti, The physics of El Niño, *Physics World*, *9*, 41–47, 1998.

Deser, C., M. A. Alexander, S.-P. Xie, and A. S. Phillips, Sea surface temperature variability: Patterns and mechanisms, *Annu. Rev. Marine. Sci.*, (2), 115–143, 2010.

Domeisen, D. I., C. I. Garfinkel, and A. H. Butler, The teleconnection of ENSO to the stratosphere, *Reviews of Geophysics*, *57*, 5–47, doi:10.1029/2018RG000596, 2019.

García-Serrano, J., C. Cassou, H. Douville, A. Giannini, and F. J. Doblas-Reyes, Revisiting the ENSO teleconnection to the Tropical North Atlantic, *J. Clym.*, *30*, 6945–6957, 2017.

Guilyardi, E., A. Wittenberg, A. Fedorov, M. Collins, C. Wang, A. Capotondi, G. J. V. Oldenborgh, and T. Stockdale, Understanding El Niño in ocean-atmosphere general circulation models: progress and challenges, *Bull. Amer. Meteor. Soc.*, pp. 325–340, 2009.

Hazeleger, W., et al., EC-EARTH v2.2: description and validation of new seamless earth system prediction model, *Clim. Dyn.*, doi:10.1007/s00382-011-1228-5, 2011.

Ineson, S., and A. A. Scaife, The role of the stratosphere in the european climate response to El Niño, *Nat. Geos. Lett.*, *2*, 32–36, doi:10.1038/NGEO381, 2009.

Klein, S. A., B. J. Soden, and N.-C. Lau, Remote sea surface temperature variations during ENSO: Evidence for a tropical atmospheric bridge, *J. Clym.*, *12*, 917–932, 1999.

Kurcharski, F., F. Ikram, F. Molteni, R. Farneti, I.-S. Kang, H.-H. No, M. P. King, G. Giulani, and K. Mogesen, Atlantic forcing of the Pacific decadal variability, *Clim. Dyn.*, doi: 10.1007/s00382-015-2705-z, 2015.

Madec, G., NEMO ocean engine, *Note du Pole de modélisation, Institute Pierre-Simon Laplace (IPSL)*, *27*, 1288–1619, 2008.

Palmeiro, F. M., J. García-Serrano, O. Bellprat, P.-A. Bretonnière, and F. J. Doblas-Reyes, Boreal winter stratospheric variability in EC-EARTH: High-Top vs Low-Top, *Clym. Dyn.*, *54*, 3135–3150, 2020.

Randel, W. J., R. R. Garcia, N. Calvo, and D. Marsh, ENSO influence on zonal mean temperature and ozone in the tropical lower stratosphere, *Geophys. Res. Lett.*, *36*, doi: 10.1029/2009GL039343, 2009.

Taguchi, M., Observed connection of the stratospheric Quasi-Biennial Oscillation with El Niño-Southern Oscillation in radiosonde data, *Journal of Geophysical Research*, *115*, doi: https://doi.org10.1029/2010JD014325, 2010.

Valcke, S., OASIS 3 user guide, *PRISM Tech*, (Rep 3), 64 pp, 2006.

Wang, C., Atmospheric circulation cells associated with the ENSO, *J. Clym.*, *15*, 399–419, 2001.

Wang, C., and J. Picaut, Understanding ENSO physics-a review, *Rev. Geophys.*, *147*, 21–48, 2004.

Webster, P. J., and H. R. Chang, Equatorial energy accumulation and emanation regions: impacts of a zonally varying basic state, *J. Atmos. Sci.*, *45*, 803–829, 1988.

Yang, C., H. M. Christensen, S. Corti, J. von Hardenberg, and P. Davini, The impact of stochastic physics on ENSO in the EC-EARTH coupled model, *Clim. Dyn.*, doi: 10.1007/s00382-019-04660-0, 2010.

Appendix

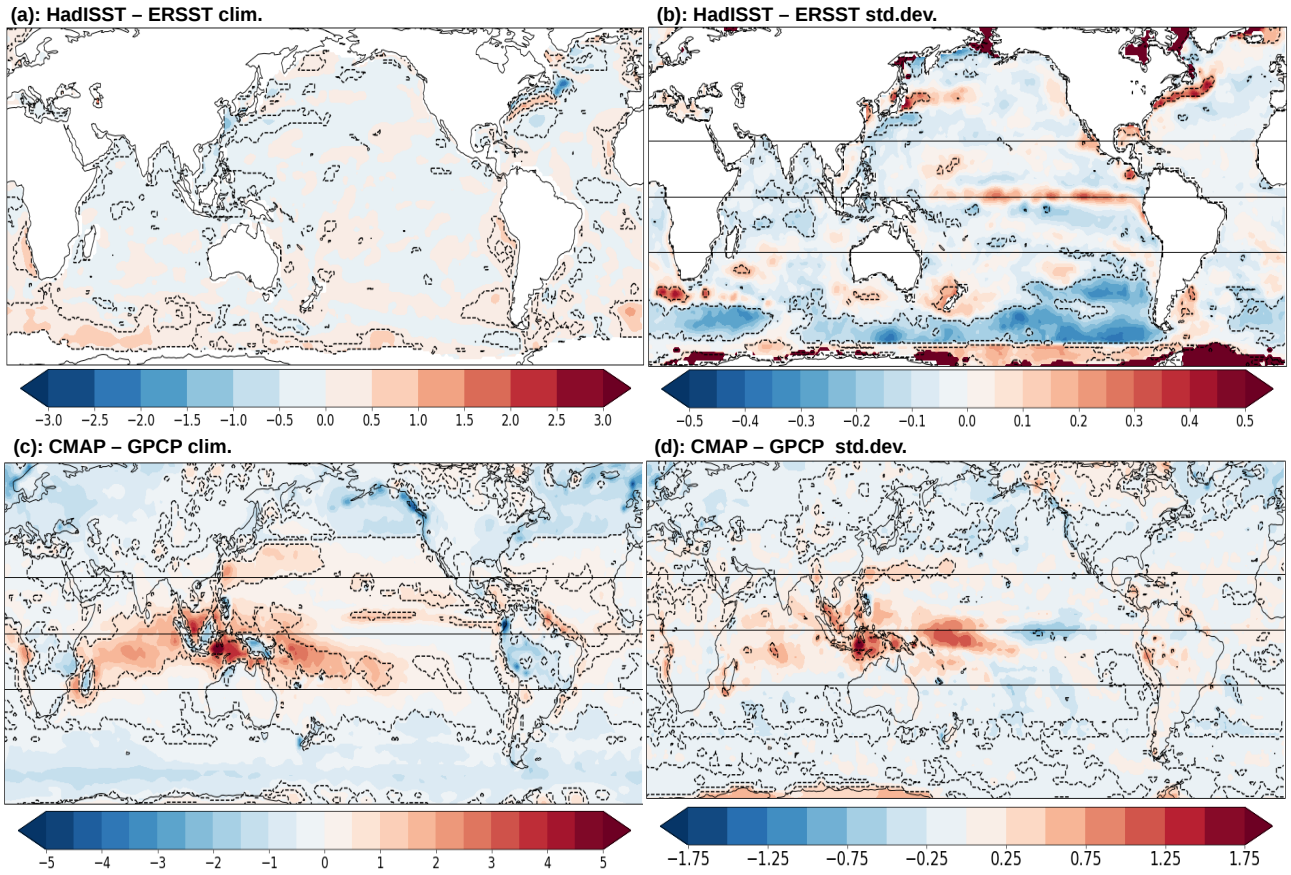

Figure 8. *(a) and (b) HadISST minus ERSST DJF climatology and standard deviation, respectively; (c) and (d) CMAP minus GPCP climatology and standard deviation. Statistical tests and color-bars are the same as in Fig.3. Solid horizontal lines are the equator and both tropics.*

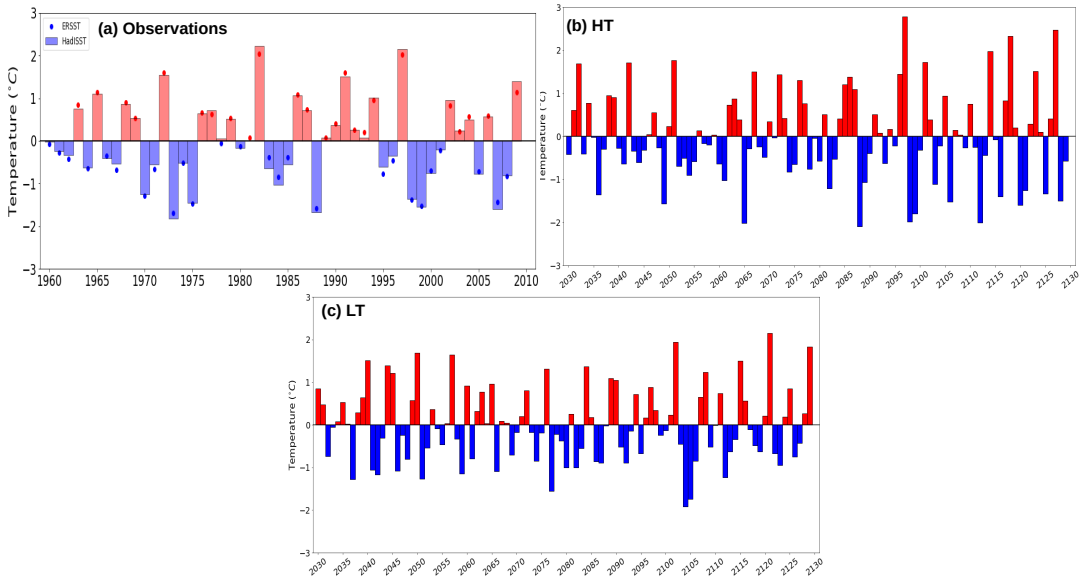

Figure 9. *Niño3.4 DJF time series for observations (a), HT (b) and LT (c).*

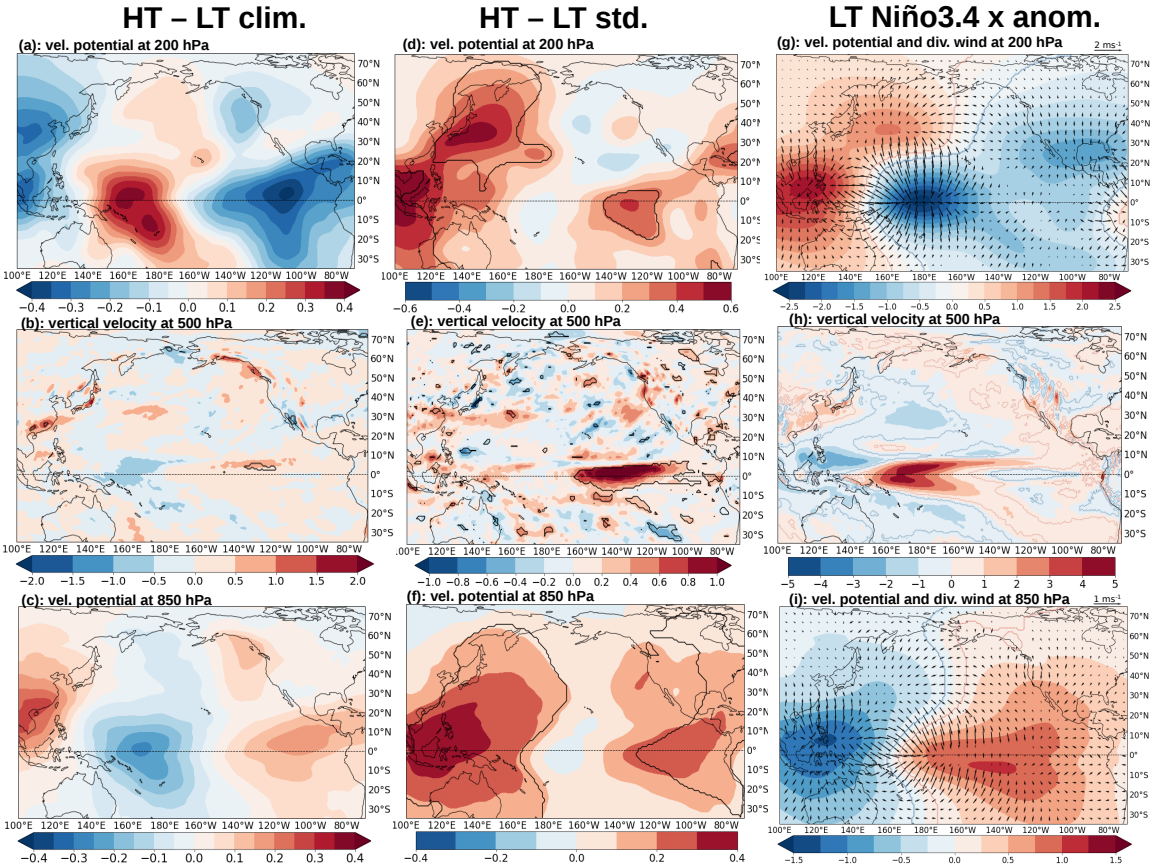

Figure 10. *(a), (b) and (c) HT minus LT DJF climatology of 200 hPa velocity potential ($10^6\ m^2 s^{-1}$), 500 hPa vertical velocity ($10^{-2}\ Pas^{-1}$) and 850 hPa velocity potential ($10^6\ m^2 s^{-1}$), respectively. (d), (e) and (f) as (a), (b) and (c) but for the standard deviation. (g), (h) and (i) as in Fig.7d, 7e and 7f, but for LT. Regions where the difference in climatology or standard deviation are statistically significant are inside contours according to a Student test and a Fisher test, respectively.*

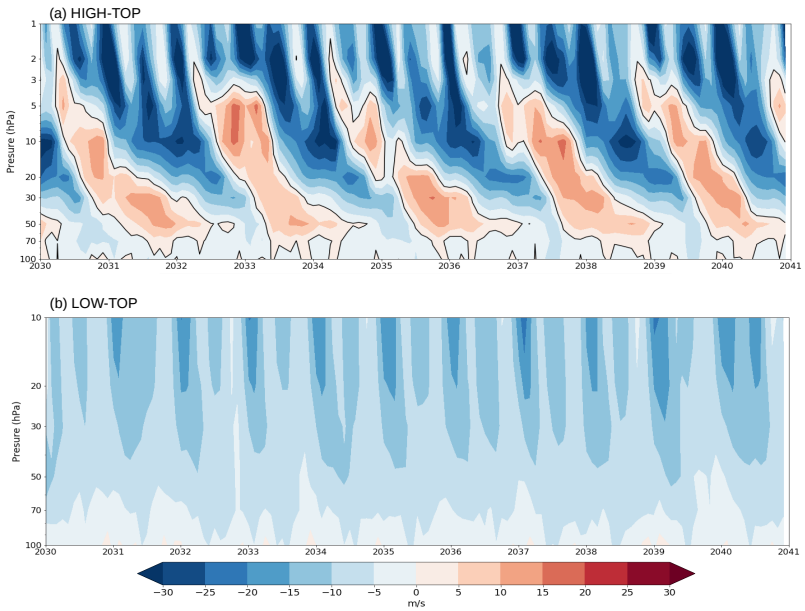

Figure 11. *Cross height-time evolution of the equatorial zonal mean zonal wind in a monthly basis for the first 11 years in HT (a) and LT (b).*